

Abstract

Evolution of solar active regions (ARs) is directly related to the occurrence of flares and coronal mass ejections. In this sense, changes in AR magnetic field can be used to unveil other relevant features like plasma flows in the region and vertical Poynting flux into the overlying atmosphere. Here, surface 3D vector magnetic field observations from SDO/HMI are studied with the differential affine velocity estimator for vector magnetograms (DAVE4VM) to recover 3D plasma flows in the photosphere. From these results, the evolution of vertical Poynting flux is presented over the lifetimes of several ARs that display differing Mt. Wilson magnetic classifications.

Introduction

In this work, the vertical Poynting flux and Mt. Wilson classification of 16 ARs are studied with the following objectives:

1. Compare both normal and tangential Poynting flux components with AR Mt. Wilson magnetic classification and area coverage as they pass over the solar disk;
2. Study how extracting Poynting flux from different parts of the ARs can impact the comparisons mentioned above.

Data and Methodology

We use Solar Dynamics Observatory (SDO) Helioseismic and Magnetic Imager (HMI) (Scherrer 2012) vectormagnetic observations from the SHARP series (hmi.sharp_cea_720s). The differential affine velocity estimator for vector magnetograms (DAVE4VM; Schuck 2008) is then used to estimate 3D velocity fields. In this work we implemented a Python version of DAVE4VM.

After obtaining the 3D velocity components these can be combined with the vectormagnetic field components to calculate the vertical Poynting flux. Considering a plane S , the vertical Poynting flux can be described as (Kusano 2002),

$$\vec{S} = \frac{1}{\mu_0} \int_S \vec{B} \times (\vec{v} \times \vec{B}) \cdot \hat{n} dS = \vec{S}_t + \vec{S}_n, \quad (1)$$

that can be split into the component due to tangential (i.e., horizontal) motions and flux emergence,

$$\vec{S}_t = -\frac{1}{\mu_0} \int_S (\vec{v}_t \cdot \vec{B}_t) \vec{B}_n \cdot \hat{n} dS, \quad (2)$$

$$\vec{S}_n = \frac{1}{\mu_0} \int_S B_t^2 \vec{v}_n \cdot \hat{n} dS. \quad (3)$$

The dataset contains ARs with different Mt. Wilson classifications distributed similarly to what usually is observed in the Sun over a whole solar cycle, but with the addition of some extra regions with higher complexity (as shown in Figure 1). Throughout this work we present the daily average of vertical Poynting flux values that have been calculated at the native data cadence of 12 minutes.

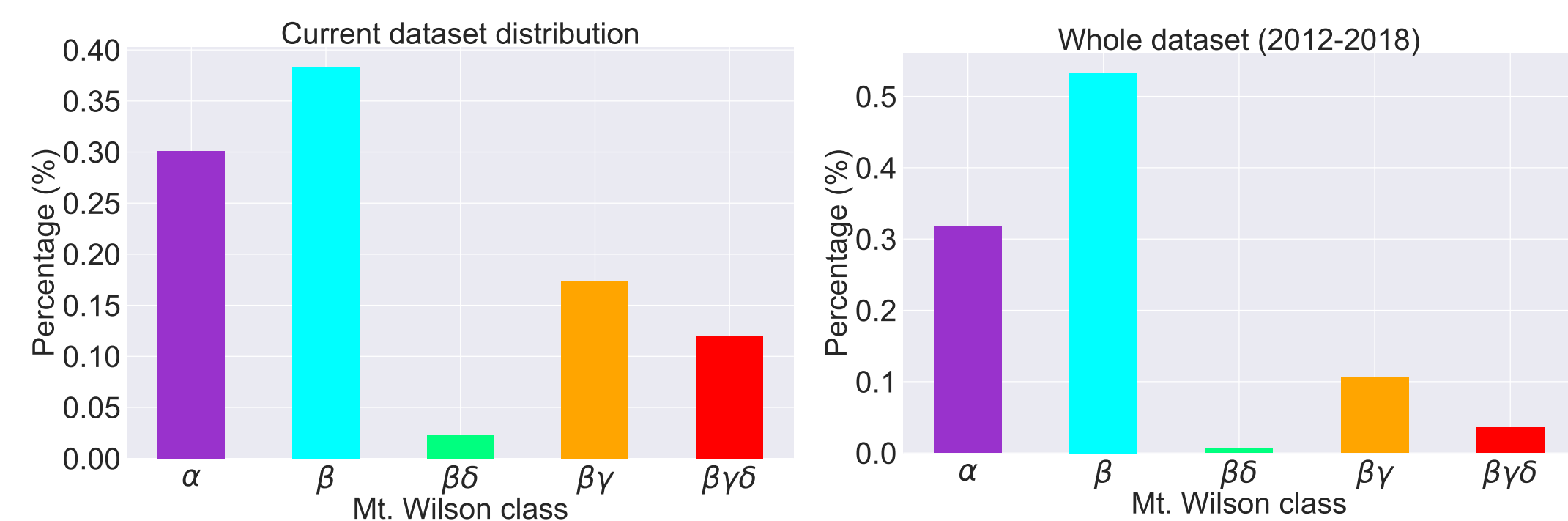


Figure 1: Mt. Wilson class distribution for each daily entry on our dataset (left) and on all SWPC entries over 2012-2018. The colour code adopted for the different Mt. Wilson classes is maintained over the next plots presented on this poster.

Results

Figure 2 compares the 24h average of normal and tangential Poynting flux components integrated over the whole HARP image space, indicating that the values are distributed slightly differently for each class. From the interquartile ranges (colored boxes) we can see that α regions tend to have considerably less energy injection in the normal component (Fig. 2 left) than $\beta\gamma\delta$ regions. However, for all Mt. Wilson classes the tails of the distributions (indicated by the whiskers) can still reach comparable values. The tangential component (Fig. 2 right) does not display the same distinction across Mt. Wilson classes.

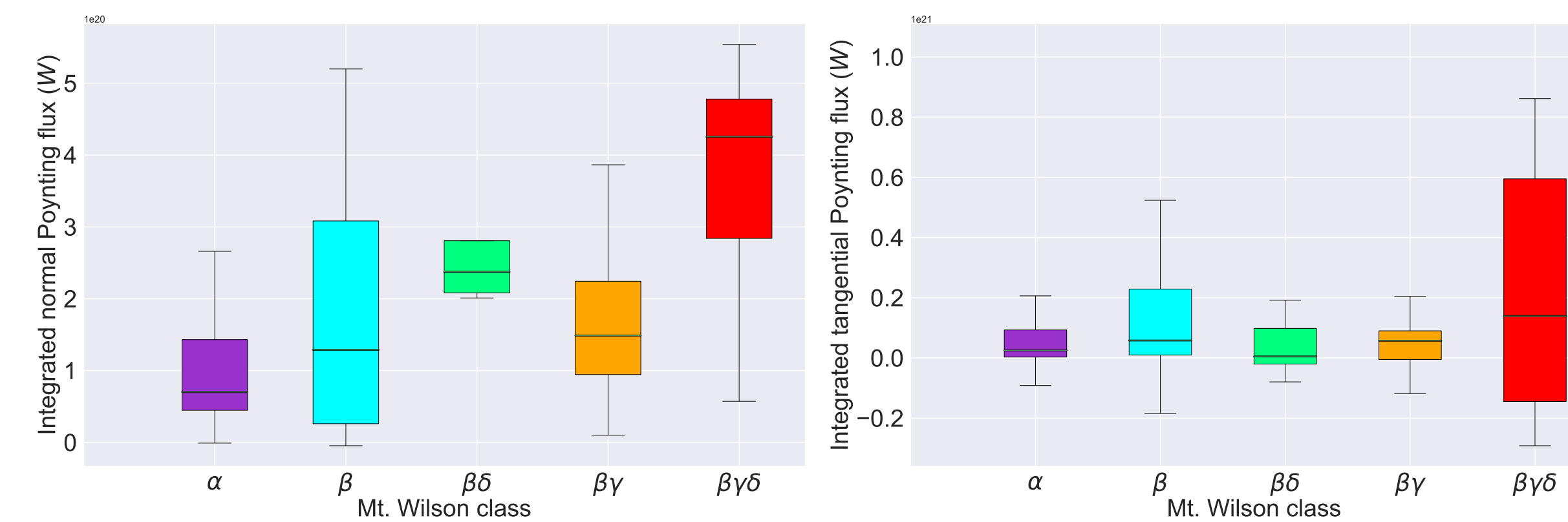


Figure 2: Box plots of the normal (left) and tangential (right) components of the vertical Poynting flux. The colour code follows that of Figure 1.

The concentration of energy injection can be observed by comparing the Poynting flux values with the area considered for integration (Figures 3 and 4 in the right-hand poster column). For this we have selected three different approaches to define the area of integration of the bitmap files from each HARP:

- **unfiltered** – the whole HARP field of view;
- **BC area** – weak and strong field area inside AR’s smooth bounding curve (BC);
- **active pixels** – strong field area inside the AR’s smooth bounding curve.

Note that for the same AR the size of the HARP field-of-view does not change within the cea data series. The results obtained in Figure 3 show that larger and more complex regions tend to experience a greater energy injection in both vertical Poynting flux components, with the exception of one AR. This may be expected for an integrated quantity, but it is worth recalling that both components are signed quantities. Figure 4 represents a first attempt to mitigate this area of integration effect by displaying the average Poynting flux of the respective areas considered. Also, it can be seen in both Figures 3 and 4 that how these values are distributed can be severely impacted depending on the portion of the AR we consider in the image space.

Conclusions

- \vec{S}_n and \vec{S}_t have values which are generally comparable in magnitude.
- ARs with more complex magnetic structure (Fig. 2) and larger area (Fig. 3) tend to present the largest values for integrated Poynting flux.
- The extreme values in the tails of the β region distribution can have as much integrated normal Poynting flux than their more complex counterparts.
- Only one day of one AR’s transit presented a negative integrated normal Poynting flux.
- The tendency for magnetically more complex ARs to have a stronger integrated Poynting flux disappears from the normal and significantly diminishes from the tangential when considering average Poynting flux.

Although not shown here, a temporal analysis of the ARs indicates:

- the tangential component tends to change sign as the AR passes over the disk, which may be an indicative that the solar rotation is contaminating the data;

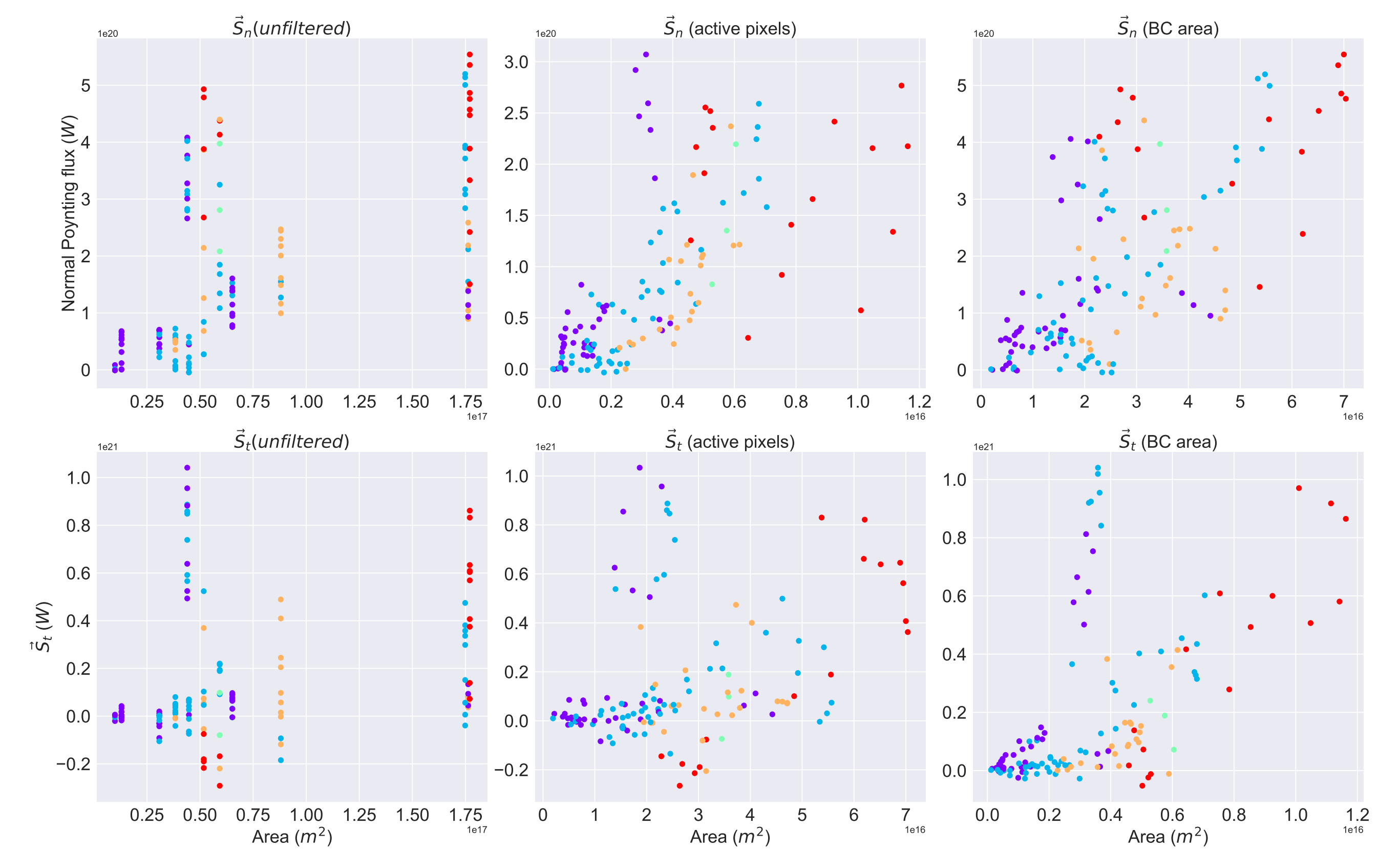


Figure 3: Normal (Top) and Tangential (Bot) Poynting flux components as a function of the integration area. Data point colour code follows Figure 1.

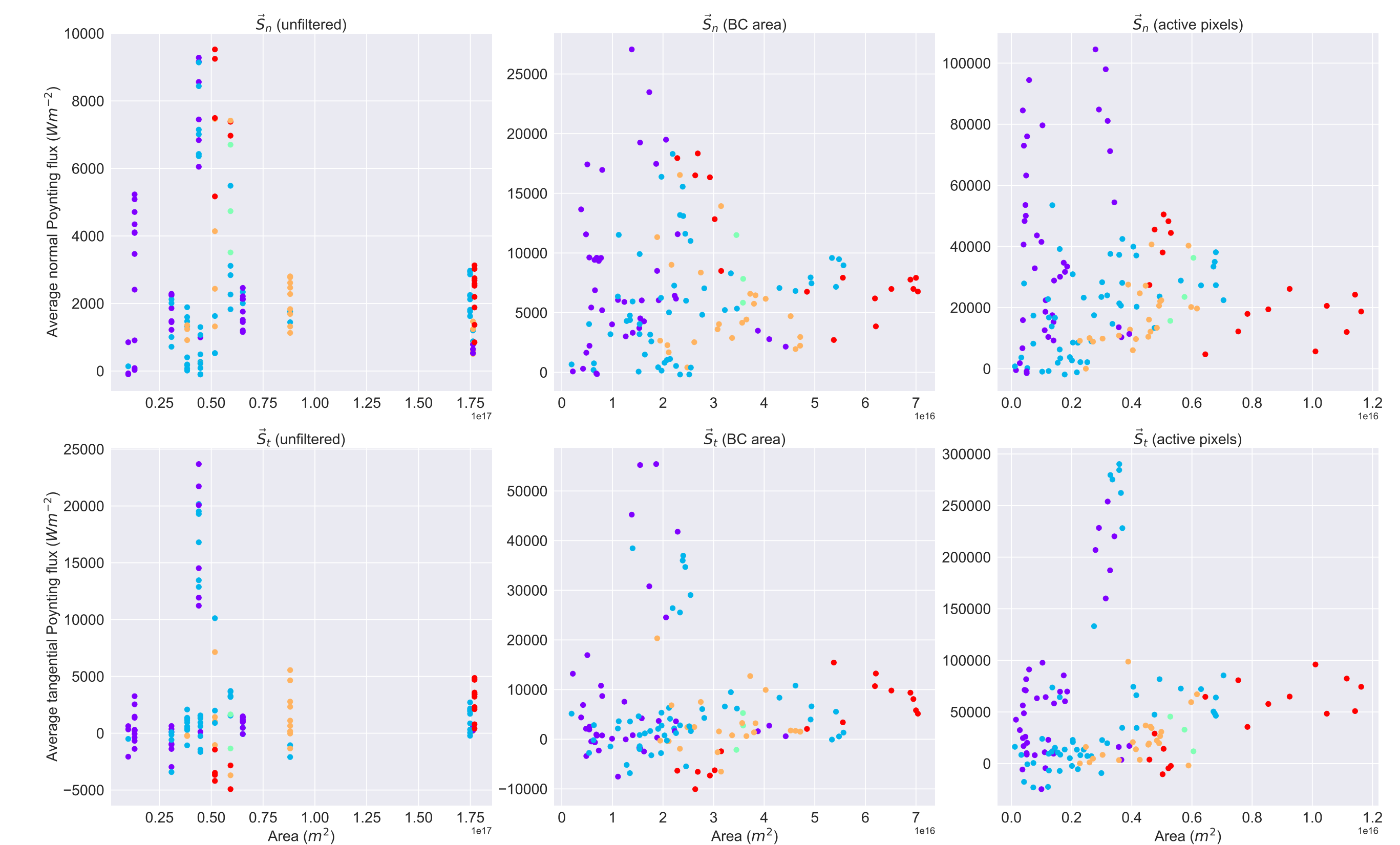


Figure 4: Normal (Top) and Tangential (Bot) Poynting flux components divided per area as a function of the integration area itself. Data point colour code follows Figure 1.

References

Kusano et al. 2002, *ApJ*, **577**, 501
Scherrer et al. 2012, *SolPhys*, **275**, 207
Schuck 2008, *ApJ*, **683**, 1134

Acknowledgements

Data are provided courtesy of NASA/SDO, the HMI science team and NOAA/SWPC. AC is supported by a Northumbria University RDF Studentship. Special thanks to the SunPy team.

Poster file and

Jupyter Notebook:

